Article

X-ray and Synchrotron FTIR Studies of Partially Decomposed Magnesium Borohydride

Rashmi Dahal [1,†], Jenny G. Vitillo [2], Anna C. Åsland [1,‡], Christoph Frommen [3], Stefano Deledda [3] and Olena Zavorotynska [1,*]

1 Department of Mathematics and Physics, University of Stavanger, P.O. Box 8600, NO-4036 Stavanger, Norway
2 Department of Science and High Technology and INSTM, Università degli Studi dell'Insubria, Via Valleggio 9, I-22100 Como, Italy
3 Department for Hydrogen Technology, Institute for Energy Technology, P.O. Box 40, NO-2027 Kjeller, Norway
* Correspondence: olena.zavorotynska@uis.no
† Current affiliation: Nuclear Material and Engineering (NuME) Group, Department of Applied Physics, Aalto University, Otakaari 1, 02150 Espoo, Finland.
‡ Current affiliation: Center for Quantum Spintronics, Department of Physics, Norwegian University of Science and Technology (NTNU), NO-7491 Trondheim, Norway.

Abstract: Magnesium borohydride ($Mg(BH_4)_2$) is an attractive compound for solid-state hydrogen storage due to its lucratively high hydrogen densities and theoretically low operational temperature. Hydrogen release from $Mg(BH_4)_2$ occurs through several steps. The reaction intermediates formed at these steps have been extensively studied for a decade. In this work, we apply spectroscopic methods that have rarely been used in such studies to provide alternative insights into the nature of the reaction intermediates. The commercially obtained sample was decomposed in argon flow during thermogravimetric analysis combined with differential scanning calorimetry (TGA-DSC) to differentiate between the H_2-desorption reaction steps. The reaction products were analyzed by powder X-ray diffraction (PXRD), near edge soft X-ray absorption spectroscopy at boron K-edge (NEXAFS), and synchrotron infrared (IR) spectroscopy in mid- and far-IR ranges (SR-FTIR). Up to 12 wt% of H_2 desorption was observed in the gravimetric measurements. PXRD showed no crystalline decomposition products when heated at 260–280 °C, the formation of MgH_2 above 300 °C, and Mg above 320 °C. The qualitative analysis of the NEXAFS data showed the presence of boron in lower oxidation states than in $(BH_4)^-$. The NEXAFS data also indicated the presence of amorphous boron at and above 340 °C. This study provides additional insights into the decomposition reaction of $Mg(BH_4)_2$.

Keywords: hydrogen storage; magnesium borohydride; soft X-ray absorption spectroscopy; boron K-edge; synchrotron FTIR

1. Introduction

Hydrogen is the energy that fuels the sun and other stars. With the potential of low-carbon production from renewable energies, and with the largest energy content by weight among chemical fuels, hydrogen is considered to be one of the most likely pillars for future economies [1,2]. At the same time, being the lightest and the least dense amongst the fuels, hydrogen gas requires significant compressing for storage and transportation. Currently, molecular hydrogen is mostly stored in liquid and pressurized forms that brings about issues of energy losses, safety risks, and expensive composite storage tanks. The idea of solid-state hydrogen storage is a lucrative alternative to overcome the challenges [3–8]. In this storage method, hydrogen is chemically incorporated in a lattice of a compound with the volumetric hydrogen densities often higher than those in liquid molecular hydrogen (71 g·L^{-1}). Most of these compounds are stable at room temperature (RT) and above, thus

bypassing the need for cryocooling. Moreover, they can be formed at pressures lower than those currently utilized in the hydrogen storage tanks (350–700 bar).

In this context, magnesium borohydride ($Mg(BH_4)_2$) is recognized as an attractive hydrogen storage compound due to its high hydrogen content (14.9 wt%, 82–147 g_{H2}/L), and relatively low H_2 release temperature that has the potential to be further reduced. In particular, experiments show that the decomposition onset of $Mg(BH_4)_2$ requires temperatures of at least 200 °C in order to break the rather strong B-H bonds [9,10]. However, H-D isotopic exchange studies have shown that the B-H bond in $Mg(BH_4)_2$ can be perturbed at temperatures as low as around 100 °C and pressure of 3 bar H_2 [11,12].

The decomposition reaction of $Mg(BH_4)_2$ suggests multiple steps with amorphous intermediate reaction products [13–19]. $Mg(BH_4)_2$ exists in multiple phase polymorphs. If the decomposition starts from the γ-phase, for example, as in the present work, two phase transitions between 145–215 °C are observed prior to decomposition [20]. At temperatures between 215–330 °C, the first hydrogen desorption is observed with the production of amorphous B-H species. In the next stage, the formation of crystalline MgH_2 takes place between 340–355 °C, which is then followed by the formation of (i) amorphous boron (B) at a temperature between 355–372 °C and (ii) MgB_2 from 372–420 °C. As suggested by Guo et al. [13], the undesirable by-product diborane can form at about 280 °C along with various amorphous B-H species and desorbed H_2 that can interact with each other in multiple steps during the decomposition reaction. Most studies indicate an approximately correct theoretical weight loss for the completely decomposed $Mg(BH_4)_2$, except for decomposition in a high dynamic vacuum [18], that rules out the stochiometric release of undesirable borane gaseous products. Some researchers suggest the formation of $MgB_{12}H_{12}$ [21] and similar higher borane compounds that would hinder rehydrogenation and reversibility, although these have not been observed consistently. The formation of $Mg(B_3H_8)_2$ was also suggested [9,22]. However, for most alkali- and alkaline-earth borohydrides, the triborane, $B_3H_8^-$, decomposes to borohydride, BH_4^-, and not vice versa [23]. It was found that the presence of an additional hydrogen source, such as MgH_2, is essential for the selective $BH_4 \rightarrow B_3H_8$ reaction. In the absence of MgH_2, $Mg(B_3H_8)_2$ does form, but in lower amounts. A recent theoretical study accessed thermodynamic stabilities and the intrinsic strengths of various intermediates in the decomposition of borohydrides, emphasizing their decisive role in hydrogenation and dehydrogenation reactions [24]. Thus, the decomposition pathway of $Mg(BH_4)_2$ has been extensively studied through the past decade, adding knowledge of its hydrogen storage properties. The consensus on the decomposition pathway and the nature of the decomposition products has not been reached.

Rehydrogenation of completely decomposed $Mg(BH_4)_2$ requires high temperature (<400 °C), high H_2 pressure (950 bars), and long reaction time (72 h) and yields > 11 wt% of H_2 [25]. However, the decomposed $Mg(BH_4)_2$ at the step of the amorphous intermediates can be rehydrogenated at comparatively lower temperatures between 250 and 285 °C, pressure of 120 bar H_2, and shorter reaction times. In this case, about 3 wt% can be cycled for at least three cycles [19]. This amount is lower than the weight loss observed for the decomposition step in this temperature range. One of the reasons behind the incomplete rehydrogenation at this step might be the formation of several decomposition products, only some of them being reversible back to $Mg(BH_4)_2$. The formation of MgO at the expense of $Mg(BH_4)_2$ might also be responsible for the reduced reversibility [26]. Therefore, to enhance the release of H_2 on reversibility, it is important to understand the nature of the intermediate amorphous reaction products.

Decomposition and rehydrogenation reactions in hydrides have been typically studied with diffraction techniques in combination with thermogravimetric and calorimetric studies (TGA-DSC). The first method is an excellent approach that allows us to determine the phase composition and crystal structure of the crystalline phases in the samples. In situ studies, in particular at synchrotron radiation facilities, allow for the following changes with sub-minute time resolution in wide temperature and hydrogen pressure ranges. The TGA-DSC methods allow us to differentiate between various thermally induced events, for

example, phase transitions, melting, and decomposition steps, and to evaluate the amount of released gaseous products as well as to assess the thermodynamic and kinetic aspects of the reactions. This combination of the two is, however, not usually sufficient to characterize the reactions with amorphous intermediates. Thus, other techniques, in particular various spectroscopies combined with DFT calculations, have been applied for additional structural characterization of the decomposition of $Mg(BH_4)_2$ and similar compounds. Vibrational spectroscopies, such as Raman scattering, Fourier-transformed infrared (FTIR) and inelastic neutron scattering (INS), identify molecular bonds and lattice vibrations. The majority of the FTIR studies on $Mg(BH_4)_2$ report the data in the mid-infrared (mid-IR) region as summarised by us earlier [10]. Vitillo et al. also presented far-infrared (far-IR) data at room temperature [18]. Pure $Mg(BH_4)_2$ exhibits well-defined and described IR spectra. The ex situ mid-infrared measurements of the amorphous decomposition products showed broad features in the B-H bending and stretching regions partially leading to inconclusive results [18,19,26]. Measurements at lower temperatures might reduce thermal effects and narrow the absorption bands. Our attempts to access these phases with in situ (and ex situ) Raman spectroscopy revealed strong fluorescence of the samples with 532 nm [20], but also with 457, 633, and 785 nm laser wavelengths (unpublished results). X-ray absorption spectroscopy (XAS) is also a suitable tool to study the local order around a chosen element. XAS has, at times, been applied to follow the local structure of additive, catalysts and dopants in $Mg(BH_4)_2$ upon H_2 desorption and absorption reactions [19,27]. In this case, the elements of interest are mostly transition metals, and hard X-rays are employed with rather simple experimental set-ups and good quality results. XAS measurements at B K-edge of the decomposition phases of $Mg(BH_4)_2$ and other borohydrides are scarce, although they could shed more light onto the local structure of boron anions in hydrogenation and dehydrogenation reaction products. The reason for this is the use of soft X-rays and an ultra-high vacuum for the most typical experimental setups, posing notable experimental challenges. In addition, $Mg(BH_4)_2$ is air-sensitive and special care must be taken in order to not introduce contamination during the sample preparation and transfer or into the measurements. Ray et al. have studied the H_2 adsorption reaction in MgB_2 with B K-edge XAS but found only direct formation of BH_4^- anions, which is certainly not the case of the reverse dehydrogenation reaction [28]. In the subsequent work, the team investigated the decomposition of $Mg(BH_4)_2$ with B K-edge XAS and concluded that γ-$Mg(BH_4)_2$ followed multiple reaction pathways in both the dehydrogenation and rehydrogenation processes [29]. Sahle et al. [30] employed inelastic X-ray scattering at the B and Mg edges for in situ studies of $Mg(BH_4)_2$ decomposition. They observed the formation of reaction intermediate(s) at 300 °C upon hydrogen release without the occurrence of stable boron compounds such as amorphous boron or $MgB_{12}H_{12}$. Higher boranes and MgH_2 were found between 300 °C and 400 °C with the boron atoms in similar electronic states to that in $B_{12}H_{12}$ anions, with subsequent decomposition into the constituting elements afterwards.

The described knowledge gaps in the nature of boron-based amorphous intermediates prompted the current study. In this work, the reaction products formed at different reaction steps during the partial decomposition of γ-$Mg(BH_4)_2$ in the temperature range 240–400 °C have been studied by using combined thermogravimetric analysis and differential scanning calorimetry (TGA-DSC), powder X-ray diffraction (PXRD), and synchrotron-based in situ FTIR (SR-FTIR) and X-ray absorption spectroscopy (XAS), in order to identify the intermediate reaction products in the decomposition reaction of γ-$Mg(BH_4)_2$. We measured these samples with SR-FTIR in the mid-IR and far-IR regions at cryogenic temperatures with the aim of solving the problem of peak broadening in the *RT* FTIR spectra and enable comparison of the results with the theoretically predicted spectral modes of various B_xH_y clusters [18,24]. The far-IR spectra of H_3BO_3 (boric acid) are reported here, to the best of our knowledge, for the first time and can be used as a reference for future studies in the related compounds. X-ray absorption spectra are expected to shed more light on the local structure of boron atoms in the intermediate decomposition phases of $Mg(BH_4)_2$.

2. Materials and Methods

Commercial gamma magnesium borohydride (γ-$Mg(BH_4)_2$) (Sigma-Aldrich, St. Louis, MO, USA, 95%) was used to prepare the samples.

Amorphous boron powder (B) (purity >95%, sigma-Aldrich), boric anhydride (B_2O_3,) (>99.98, Sigma-Aldrich), magnesium boride powder (MgB_2) (>99%, boric acid (H_3BO_3) (ACS reagent, >99.5%, Sigma-Aldrich), and lithium borohydride ($LiBH_4$) (>90%, Sigma-Aldrich) were used as references.

Thermogravimetric analysis combined with differential scanning calorimetry (TGA-DSC): partially decomposed samples of $Mg(BH_4)_2$ were obtained by heating the as received compound at different decomposition temperatures between 240–400 °C in the instrument for thermogravimetric analysis combined with differential scanning calorimetry TGA/DSC 3+ from Mettler Toledo. The samples were heated at 5 °C/min up to the required temperature and then left to decompose isothermally until no weight loss was observed. The experiments were carried out in Ar flow of 200 mL per minute in alumina (Al_2O_3) crucibles with pierced lids. The sample was filled into crucibles inside a glove box and transferred into the TGA-DSC that was placed outside the glove box within a few seconds.

Powder X-ray diffraction (PXRD) data were collected at a Bruker D8 Advance diffractometer with copper X-ray source of wavelength (λ) 1.5418 Å. The samples were sealed in glass capillaries whilst inside an Ar atmosphere, and measured in the range 2θ = 11–60° with a constant rotation rate of 120 rpm. Data were collected in steps of 0.01° with 0.2 s per step.

Synchrotron X-ray absorption spectroscopy (XAS) data were collected at the dipole magnet RGBL beamline at the Helmholtz-Zentrum Berlin für Materialien und Energie synchrotron radiation facility (Berlin, Germany). The samples were loaded onto stainless-steel sample holders covered by indium tape inside the Ar-filled glove box. Then, they were transferred into the measurement chamber without contact with air. The measurements were performed in an ultra-high vacuum, in total electron yield (TEY) mode. The samples were measured at 45° to the X-ray beam, in 160–260 eV range with 0.4–0.5 eV resolution and 10 s per step.

The experimental values were obtained as the total electron yield (TEY). Incident flux, I_0, was obtained from the measurements of reference Au foil: (i) the measured TEY from the Au foil was normalized to the ring current, (ii) the TEY Au signal was normalized to the absorption cross-section of gold:

$$flux(I_0) = \frac{TEY(Au)}{\{ring\ current\} \cdot \sigma_a^{Au}}$$

Once (I_0) was obtained, the total absorption cross-section for the sample (σ_a^{sample}) was calculated by dividing the normalized TEY of the sample to the ring current by the incident $flux(I_0)$ as given below:

$$\sigma_a^{sample} = \frac{TEY(Sample)}{\{ring\ current\ sample\} \cdot flux(I_0)}$$

Next, the absorption cross-section for each sample was modified by subtracting the user-defined background by taking some points from the pre-edge and the post-edge region of the spectrum. The intensity of the spectrum thus obtained was then normalized between [0, 1] to get the final spectrum.

Synchrotron Fourier-transformed infrared spectroscopy (SR-FTIR) were performed at IRIS beamline of the the Helmholtz-Zentrum Berlin für Materialien und Energie synchrotron radiation facility (Berlin, Germany). A first set of mid-IR and far-IR spectra was recorded in the temperature range RT-10 K on: (i) two reference materials: H_3BO_3 and $Mg(BH_4)_2$; and (ii) $Mg(BH_4)_2$ decomposed at 260 °C and 280 °C. The samples were diluted in CsI for the mid-IR measurements and in wax for the far-IR measurements. The mid-IR spectra were obtained with the globular source of a Bruker Vertex instrument whereas a

synchrotron beam was used to record the far-IR spectra. Every spectrum was obtained with a spectral resolution of 4 cm^{-1} averaging 1024 scans. All the pellets have been prepared in a MBraun glove box where the level of water and O_2 were kept <0.5 ppm and <1.5 ppm, respectively, during use but exposed to air for a short time while transferring them to the cryostat.

3. Results

3.1. TGA-DSC Analysis of Decomposition of γ-Mg(BH₄)₂

The TGA-DSC profiles of the γ-Mg(BH₄)₂ decomposition in Ar flow are presented in Figure 1 and indicate the following:

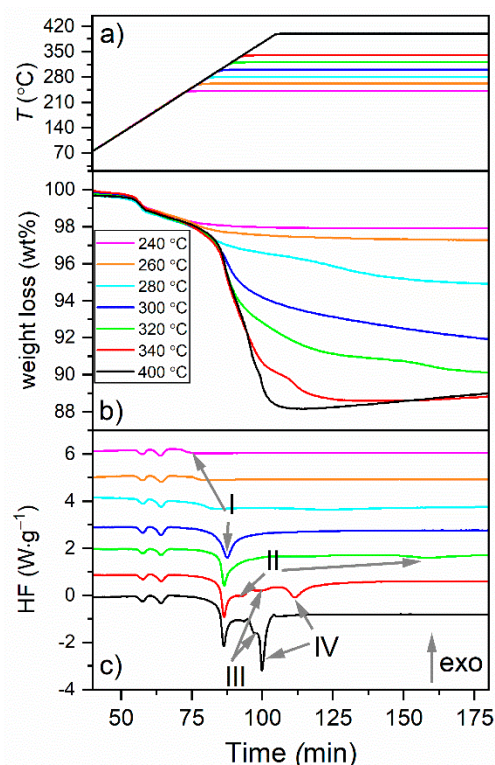**Figure 1.** (**a**) Temperature, (**b**) TGA and (**c**) DSC profiles of γ-Mg(BH₄)₂ samples kept at different temperatures in Ar flow.

The weight losses distinctively indicate several reaction steps in the decomposition reactions (Figure 1a).

- Some weight loss, ~0.5 wt%, occurred between R*T* and the phase-transition temperature region (T_{ons} = 152 °C).
- ~0.8 wt% occurred during the two phase transitions at 163 and 196 °C.
- The number of the reaction steps is the same for the 240 °C and 260 °C isotherms. The DSC profiles of these reactions show the onset of the first decomposition reaction peak (I). This peak is more pronounced in the 280 °C isotherm and is complete in the 300 °C isotherm. Thus, similar reaction products can be expected after the decomposition at 240 and 260 °C, and slightly different at 280 °C. These reaction products decompose as shown by the strong exothermic peak at 305 °C. Moreover, since a larger weight loss was observed at 260 °C than that at 240 °C, we could expect the presence of Mg(BH₄)₂ in the latter sample due to the incomplete decomposition reaction at this step. The final weight loss for reaction step I was, thus, observed as 8.8% after decomposition at 300 °C for 5 h when the step was complete.
- The DSC profile of the isotherm obtained at 320 °C shows the onset of yet another peak (II). The weight loss at this temperature was larger (9.9 vs. 8.8% than that at

300 °C) Thus, the reaction products are expected to be somewhat different after the 320 °C isotherm.

- Between 320 and 340 °C, the reaction step II was completed, and two new reactions corresponding to the thermal events III and IV occurred where the latter one was incomplete. The reaction step IV was completed during the decomposition at 400 °C. Thus, yet another and different reaction products can be expected after the decomposition after 340 and 400 °C.
- The most significant weight losses occurred during the decomposition at 300 and 340 °C. These should correspond to the formation and decomposition of MgH_2.
- The decomposition at 400 °C was not complete as it resulted in 12 wt% weight loss compared to the 14.9 wt% of the theoretical content of H_2. A significant release of borane gases is, thus, not expected because it would correspond to larger weight losses with respect to the theoretical value. As all MgH_2 was decomposed at this stage, the remaining hydrogen might be trapped in higher borane intermediates.
- Some isotherms showed weight gain at elevated temperatures. This could likely be related to oxygen contamination and formation of MgO. For these isotherms, the weight loss values (summarized in Table 5) refer to the maximum observed values.
- The TGA-DSC results are discussed in Section 4 after the analysis of the decomposition phases obtained at each of the steps.

3.2. PXRD Analysis of the Reaction Products

The powder X-ray diffraction patterns of the starting and decomposed samples, recorded ex situ, are shown in Figure 2. The results reveal the absolute prevalence of γ-$Mg(BH_4)_2$ in the starting material, presence of ht-$Mg(BH_4)_2$ after the 240 °C isotherm [20], but no crystalline phases after decomposition at 260 °C. MgH_2 appeared at 300 °C, though traces can be distinguished already after 280 °C, and decomposed into Mg after 320 and 340 °C. In addition, MgO was observed in the patterns of the samples treated at and above 320 °C. A broad background that might be related to amorphous phases was observed in some of the patterns.
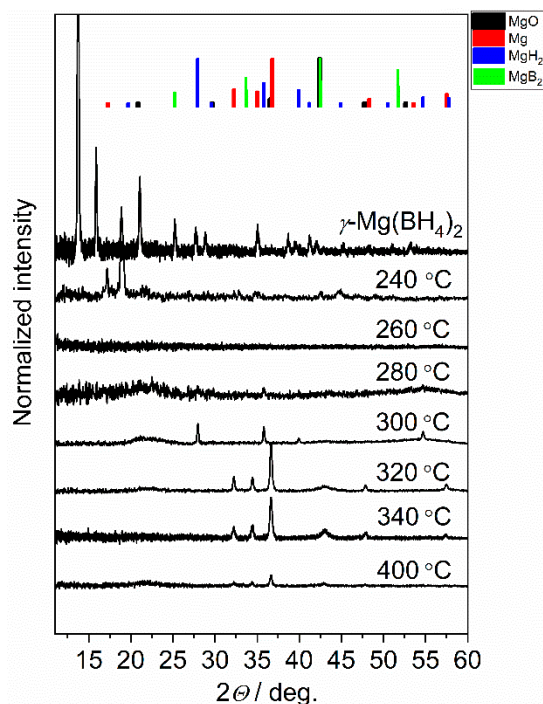

Figure 2. PXRD profiles of as received $Mg(BH_4)_2$ and the samples decomposed at various temperatures. The pattern of as received $Mg(BH_4)_2$ corresponds to the porous γ-phase, the pattern recorded after the 240 °C isotherm resembles one of the high temperature phases [20].

3.3. Synchrotron FTIR Analysis of the Decomposition Reaction Products

The samples measured with SR-FTIR included pristine $Mg(BH_4)_2$, the borohydride decomposed at 260 °C and 280 °C, and H_3BO_3 as the reference for oxygen-related impurity phases. Mid-IR and far-IR spectra, recorded at 10 K, of pristine $Mg(BH_4)_2$ and after its decomposition at 260 °C and 280 °C along with the spectrum of H_3BO_3 (blue curve) are reported in Figure 3.

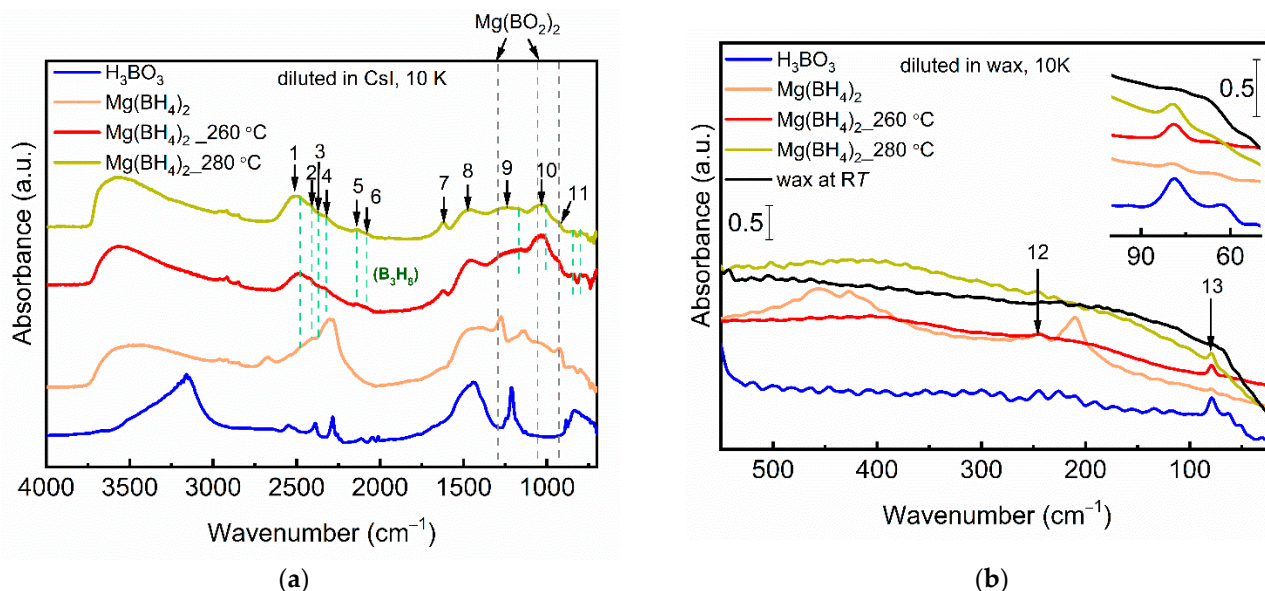**Figure 3.** (**a**) Mid-IR spectra of pristine and partially decomposed $Mg(BH_4)_2$. The spectrum of H_3BO_3 is also reported for comparison. The spectra are recorded at 10 K. The modes expected for $(B_3H_8)^-$ are illustrated according to the reference [23]; (**b**) Far-IR spectra recorded at 10 K of pristine and partially decomposed $Mg(BH_4)_2$. The spectra of H_3BO_3 and of the diluent (wax) is also reported for comparison. The inset shows the region around the band at 70 cm^{-1} associated with boric acid (borate). The assignment for the modes 1–13 is given in Table 4.

The spectra of H_3BO_3 were recorded as a reference for possible impurities. In addition, upon contamination with atmospheric water, $Mg(BH_4)_2$ can hydrolyze to $Mg(BO_2)_2$ as [31]:

$$Mg(BH_4)_2 + 4H_2O \rightarrow Mg(BO_2)_2 + 8H_2 \tag{1}$$
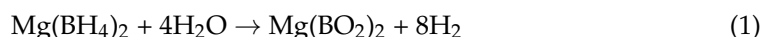
In H_3BO_3, boron atoms are surrounded by three oxygen atoms in planar coordination (three coordinated boron, B_{tri}). In magnesium diborate $Mg(BO_2)_2$, boron bonds with four oxygen atoms in tetrahedral coordination, B_{tetra}. The anion consists of two BO_4 tetrahedrons with an oxygen bridge. In tri-, tetra-, penta-, and hexaborates both B_{tri} and B_{tetra} are present in various combinations [32]. Table 1 lists the normal modes of these two anions whereas Table 2 shows the list of the peaks in experimentally observed FTIR spectra of the two compounds.

Table 1. Vibrational frequencies for the normal modes of isolated planar BO_3 (D_{3h}) and tetrahedral BO_4 (T_d) groups in crystalline state [33]. All of the frequencies are in cm^{-1}.

Group	ν_1	ν_2	ν_3	ν_4
$[BO_3]^{3-}$	1060 (R) [1]	668, 648 (IR)	1490–1428 (R, IR)	545 (R, IR)
$[BO_4]^{5-}$	880 (R)	371 (R)	886 (R, IR)	627 (R, IR)

[1] R—Raman active, IR—infrared active.

Table 2. FTIR features of H_3BO_3 (planar B_{tri}-O groups) and $Mg(BO_2)_2 \cdot 3H_2O$ (tetrahedral B_{tetra}-O groups) [32] in comparison with our data for H_3BO_3. All of the frequencies are in cm^{-1}.

H_3BO_3	$Mg(BO_2)_2 \cdot 3H_2O$	H_3BO_3
Ref. [32]	Ref. [32]	This work
	3571, vs [1]	
	3491, vs	
3202, br	3179, vs	3160 vs, br
2515, m	2531, m	2550 m, br
2362, m		2388 m
2262, s		2283 m
2030, w		2046–2010 w
1423 (ν_3) [2], s, br		1448 vs, br
	1297, vs	1245 w
	1221, m	
1193 (ν_3?), vs	1163, vs	1212 vs
	1042, vs	
	953, vs	
883, m	873 (ν_3), vs	886 m
811, m	802, w	815 m, br
644 (ν_2), s		
546 (ν_4), vs	586 (ν_4), vs	550, s
n/a		79, m

[1] vs—very strong, s—strong, m—medium, w—weak, br—broad, sh—shoulder; [2] $\nu_{s,a}$—symmetric, asymmetric stretching; δ—bending; data are from ref. [32].

The most prominent differences between the H_3BO_3 and $Mg(BO_2)_2 \cdot 3H_2O$ are the peaks at 1423 (s) and 1193 (vs) cm^{-1} (for H_3BO_3) and 1297 (vs) and 1042 (vs) cm^{-1} ($Mg(BO_2)_2 \cdot 3H_2O$). These features are taken here as the fingerprint for the presence of such groups in the samples. The peak positions observed in the spectra of H_3BO_3 are blue-shifted with respect to the literature data. This is likely associated with the difference in the diluting matrix, CsI here and KBr in Ref. [32]. In the far-IR spectrum of H_3BO_3, only one peak is observed at 79 cm^{-1} that, due to its low energy, could be assigned to the translational motions of the whole borate unit.

The mid-IR spectrum of $Mg(BH_4)_2$ is dominated by the characteristic peaks, due to stretching and bending of B-H bonds in BH_4^- ions with distorted tetrahedral local symmetry [10]. These peaks are listed in Table 3. The symmetric stretching ν_1 is probably too weak, even though it can be observed theoretically, whereas the asymmetric stretching ν_4 is visibly split due to the symmetry distortion of the BH_4^- tetrahedra in $Mg(BH_4)_2$.

Table 3. FTIR features of γ-$Mg(BH_4)_2$ from literature and this work (orange curve on Figure 3). All of the frequencies are in cm^{-1}.

Observed Peak Refs. [10,11]	Mode	Assignment [2]	This Work
n/a	ν_1	ν_s (B-H)	—
1370, m, br [1]	ν_2	δ_s (H-B-H)	—
2270 ± 2, vs	ν_3	ν_a (B-H)	2300 s, br
1260, s	ν_4	δ_a (H-B-H)	1276 s, br
1120 ± 10, m	ν_4	δ_a (H-B-H)	1144 s, br
2660, m	$\nu_2 + \nu_4$	overtone	2672 m
434, m		Mg-B stretching	455 m, br
409, m		Mg-B stretching	425 m, br
257, 231, 208, m		B-Mg-B bending	240 w, 210 m

[1] vs—very strong, s—strong, m—medium, w—weak, br—broad, sh—shoulder; [2] $\nu_{s,a}$—symmetric, asymmetric stretching; $\delta_{s,a}$—symmetric, asymmetric bending; data and assignment are from refs. [10] (mid-IR), and [18] (far-IR).

In the far-IR spectrum of $Mg(BH_4)_2$ (Figure 3b, orange curve), only the weak feature at 79 cm^{-1} is similar to the one in H_3BO_3. Other peaks are similar to those reported earlier [18]. It can be mentioned that most of the measurements on borohydrides and similar compounds reported in the literature have been performed using attenuated total reflection (ATR) sampling, a method where no sample dilution is required. In this study, the samples were measured in the transmission mode, diluted in CsI or wax, and thus, the effect from the matrix can be expected in the spectra in addition to a slight shift of the peaks and slightly different intensity ratios between higher-energy and lower-energy modes [34]. For example, the broad absorptions at 3600–3300 with 1620 cm^{-1} (water) and the weak peaks at ca. 2900 cm^{-1} (C-H bonds of organics) are most probably related to the impurities in the matrix.

In the decomposed samples (Figure 3), the peaks due to BH_4^- disappeared to the benefit of B-H vibrations of "higher" boron hydride compounds. The peaks after decomposition at 280 °C and 260 °C are very similar and are listed in Table 4. The features of H_3BO_3 might be partially responsible for the observed peaks 8–10, however the spectra obviously contain contributions from other species. Notably, the weak features at 2130 and 2075 cm^{-1} not present in the pristine $Mg(BH_4)_2$ or H_3BO_3 / $Mg(BO_2)_2$ are suggesting that the boranes with bridged hydrogen atoms in the structure are formed at this stage. These could be $(B_2H_7)^-$, $(B_3H_7)^{2-}$ [22], $(B_3H_8)^-$ [22,35,36], $(B_4H_{10})^{2-}$ [18], etc. These peaks are accompanied by the peaks at > 2300 cm^{-1}, which are characteristic for the stretching of terminal hydrogen atoms of such boron hydride anions and Mg-H-B stretching [37].

Table 4. Experimentally observed peaks in the FTIR spectra of γ-$Mg(BH_4)_2$ decomposed at 260 °C and 280 °C. All of the frequencies are in cm^{-1}.

Peak No.	Energy, cm^{-1}	Tentative Assignment
1	2510 s, br	ν(B-H)
2	2410, s	ν(B-H)
3	2375, m	ν(B-H)
4	2320, m	ν(B-H), /ν(Mg-H-B)
5	2140, w	ν(B-H-B)
6	2075, w	ν(B-H-B)
7	1620, m	δ(H-O-H)/δ(B-H)
8	1460, s, br	ν_a(B_{tri}-O)/δ(B-H)
9	ca. 1230, br	ν_s(B_{tri}-O)/ν(B_{tetra}-O)/δ(B-H)
10	~1030, s, br	ν(B_{tetra}-O)/δ(B-H)
11	930, sh	ν(B-B)/δ(B-H)
13	79, m	T (B_{tri}-O)

There are several high-frequency peaks above and below 2400 cm^{-1} (1–4) corresponding to the stretching modes of bonds involving boron and terminal hydrogen atoms, B-H_{term}. This was observed in case of $(B_3H_8)^-$ ions that comprise different types of boron atoms: two equivalent at the base (B1) and one in the third corner (B2) of an isosceles triangle [23]. All of the three atoms have two terminal hydrogens, but the bonds have slightly different energy roughly divided in the regions above and below 2400 cm^{-1}. In CsB_3H_8, the B1-H_{term} stretching was found at 2360–2325 cm^{-1}, and the stretching of B2-H_{term} at 2405–2467 cm^{-1} [23] with 2405 cm^{-1} being the most prominent feature. The stretching of the bridged hydrogens (B-H-B) was observed at 2120 and 2080 cm^{-1}. In η^2-$Mg(B_3H_8)_2(THF)_2$, the respective absorptions were recorded at 2383, 2432 for the terminal, and 2115 and 2069 cm^{-1} for the bridged units [37]. In addition, the 2280 and 2335 cm^{-1} peaks were assigned to bridged Mg–H–B stretching. Neither work reported vibrations above 2435 cm^{-1} for the $(B_3H_8)^-$. The observed absorptions correspond well with the modes 1–6 in Table 4, but we are left with 2510 cm^{-1} unaccounted for and an absence of a feature responsible for the Mg-H-B interactions. In addition, the lower frequency modes of $(B_3H_8)^-$ might be referred from the broad absorptions in Figure 3a. However, also in this region, a few unaccounted-for modes remain. In particular, H-B-H bending modes

were observed at 1168, 1000, 802, and 782–732 cm^{-1} in ref. [23] with no peaks at 1460, or 930 cm^{-1}, as in our study. (B$_2$H$_7$)$^-$ ions have distinct features at 2405, 2050 (broad), and 1030 cm^{-1} (sharp) [38] but not in the other peaks observed here. In addition, this anion is very unstable and has only one hydrogen bridge, hence one corresponding vibration. Some boranes and borane anions, such as B$_5$H$_x$ (x = 9, 11) have strong IR absorptions in the region 1620–1400 cm^{-1} assigned to B-H bending modes [39–41]. At the same time, the stretching modes of terminal B-H in the pentaboranes are shifted to higher frequencies with respect to the modes 1,2 in Table 4 (>2548, and 2460 cm^{-1}), one of the ν(B-H-B) is located below 2000 cm^{-1} (clearly absent in Figure 3a); a few prominent lower frequency modes do not correspond well with features 9–11 from Table 4 (1164, 1043, 951, 899 cm^{-1} for B$_5$H$_{11}$ [39] and 1045–1035, 900 cm^{-1} for B$_5$H$_9$ [40]). In B$_4$H$_{10}$, the most prominent structural feature is the dual pair of bridges at 2120 cm^{-1} holding the molecule together [39]. The intensity of these modes is as strong as ν(B-H), which is certainly not the case for the weak features 5,6. The stretching of terminal B-H$_2$ is found at 2550 and 2455 in tetraborane, the prominent low-frequency absorptions include 1380 (s), 1145 (s), 1067 (m), 967 (s) cm^{-1}, and a group at 850 cm^{-1}. (B$_4$H$_{10}$)$^{2-}$ [18] is proposed as a plausible intermediate. It does not have bridged hydrogens, but its other theoretically calculated modes might correspond to the spectra observed here. The data in Table 4 does not correspond to the FTIR features of the B$_6$H$_9$$^-$ anion [41].

The broad absorption in the 2440–2630 cm^{-1} region can include stretching of B$_n$H$_n$$^{2-}$ (n = 6, 8, 9, 10, 11, 12) anions [42]. B$_9$H$_9$$^-$: 2529, 2450, and 2415 cm^{-1}, B$_{12}$H$_{12}$$^-$: 2485 (strong, s), 1071 (m), and 719 (m) cm^{-1} [43]; B$_{10}$H$_{10}$$^{2-}$ salts have a very strong absorption at 2470 cm^{-1} (equatorial B-H stretch) with a shoulder at 2530 cm^{-1} (apical B-H stretch); 1015 cm^{-1} and 1070 cm^{-1} were attributed to cage deformational (*ibid*). B$_6$H$_6$$^-$ has features at 2432, 1051, and 731 cm^{-1} [43]. In summary, closo-boranes B$_n$H$_n$$^{2-}$ (n = 6, 8, 9, 10, 11, 12) do not have peaks in the region 1200–2500 cm^{-1} [42], and at ca. 900 cm^{-1}.

In summary, the FTIR spectra of the Mg(BH$_4$)$_2$ decomposed at 260 °C and 280 °C indicate: (i) formation of the same species at both temperatures; (ii) formation of several anionic species with the most probable candidates being B$_3$, B$_5$ borohydrogens with bridged H-B-H groups; (iii) the assignment is hindered by the presence of borate impurities.

We observed two different behaviors for the mid-IR and far-IR spectra upon decreasing the temperature. In fact, while the position and FWHM of the mid-IR bands remain almost unchanged in the whole temperature range (not shown), all the far-IR signals showed a decrease in their FWHM (see Figure 4 where the effect of the temperature on the band at 70 cm^{-1} is shown).
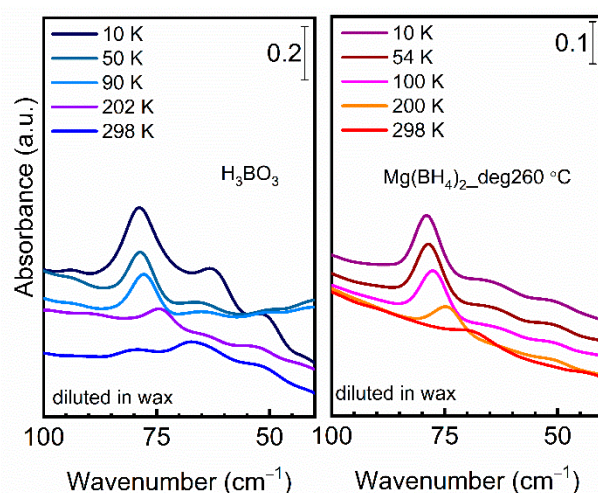

Figure 4. Temperature dependence of the far-IR spectra in the R*T*-10 K for the reference H$_3$BO$_3$ (**left**) and the Mg(BH$_4$)$_2$ decomposed at 260 °C (**right**).

Unfortunately, the extinction coefficient of the species originating from the decomposition of $Mg(BH_4)_2$ (besides borates) was so low in the far-IR region that their signal remained very broad and not so clearly distinguishable from the background also at 10 K, although we have used the highest concentration possible based on sample availability. It would be important to repeat the experiment using pure samples without any diluent.

3.4. Soft X-ray Absorption Spectroscopy at the B K-Edge of the Decomposition Products

XAS measurements were carried out with a TEY approach that is based on measuring the sample current produced by Auger and photoelectrons. For low Z-number elements and concentrated samples, the TEY mode is favorable compared to the total fluorescence yield mode (TFY) as the fluorescence becomes greater than the Auger yield of elements with Z > 30. Additionally, the TFY spectra can be distorted due to self-absorption in concentrated samples. On the other hand, the TFY method is more sensitive to bulk properties as it probes about 200 nm–5 μm Å [28], whereas the TEY method is determined primarily by the penetration ranges of Auger electrons that have ranges of tens to hundreds of nm [44]. The probed sample thickness, R_p, can be approximately determined through the relation:

$$R_p \approx 1000 \cdot E^{1.4} / \rho$$

where E is an initial electron energy in keV, ρ is the material's density in g/cm^3 and R_p is given in nm. According to this relation, the samples probed at the B K-edge energy range can be estimated as 14–28 nm for porous γ-$Mg(BH_4)_2$, 10–20 nm for the denser phases of $Mg(BH_4)_2$ and perhaps for the MgB_xH_y intermediates, and 5–11 nm for H_3BO_3, etc., i.e., in the range from a few to a few tens of nanometers.

For the qualitative data analysis, spectra of $Mg(BH_4)_2$ decomposed at various temperatures were compared with each other and the spectra of the reference compounds: boron (B), boric acid (H_3BO_3), boron oxide (B_2O_3), fresh gamma magnesium borohydride (γ-$Mg(BH_4)_2$), lithium borohydride ($LiBH_4$) and magnesium boride (MgB_2). Figure 5a,b show the experimental NEXAFS B K-edge spectra for the references and the samples, respectively. The XAS spectra of boric acid and boron oxide were analyzed as the reference for potential impurities in the spectra of $Mg(BH_4)_2$ and MgB_xH_y. In many compounds with boron in trigonal coordination and an empty $2p_z$ orbital, a strong, sharp and low energy peak has been observed due to the $1s \rightarrow 2p_z$ transition [45]. On the other hand, in high symmetry environments, such as icosahedra of elemental boron, polyhedra of borane and carborane complexes, and tetrahedral coordination, where $2p_z$ hybridization occurs, such a feature is not usually found, and the spectra are mostly characterised by a broad band at higher energy. Blau et al. [46] have proposed that NEXAFS spectra of boron with triply degenerate 2p orbitals should exhibit only one broad peak, whereas two peaks can be expected where 2p orbitals would split and $1s \rightarrow 2p_z$ transition is possible. The latter transistion should be expected as a sharp feature at a lower energy.

Thus, in B_{tri}-O planar anions, the X-ray absorption at the boron K-edge promotes $1s \rightarrow 2p_z$ (π*) electronic transitions characterized by a lower energy sharp prominent peak at 194 eV. In addition, a weak peak is observed at 197.5 eV stemming from a dipole-forbidden transition $1s \rightarrow a_1'$ σ* MO formed by B_{3s}, O_{2s} and O_{2p}. The forbidden transition activates due to the distortion of BO_3 from the perfect planar coordination as the O-B-O angles can vary in the 119.6–200.4° region. The second allowed broad feature around 198–205 eV consists of at least three distinct peaks at 200, 202 and 204 eV. They can be assigned either to the transitions of B 1s electrons to unoccupied B-O sigma antibonding (σ*) orbitals of e' ($B_{2px} + B_{2py} + O_{2s} + O_{2p}$) symmetry [47] or to B_{3p} and B_{4p} rather than 2p interactions [48]. The NEXAFS spectra of B_{tetra}-O anions are characterized by the peaks at 198 eV (strong, $B_{1s} \rightarrow$ *σ_{t2} ($B_{2p} + O_{2p}$) transition) and 200 eV ($B_{1s} \rightarrow a_1$ ($B_{2s} + O_{2p}$) transition). The broad feature at 201.5 eV may be assigned to $B_{1s} \rightarrow$ *σ_{t2} and $B_{1s} \rightarrow$ *σ_{a1} where the distortion can lift the t_2 degeneracy and cause further splitting or broadening of the peak [47]. It has been noted that even the compounds where only B_{tetra}-O should nominally be present, the features of B_{tri}-O can be observed, as this coordination is more

favorable near the surface and at defects [47,49]. The spectra of H_3BO_3 and B_2O_3 shown in Figure 5a predominantly include the features of B_{tri}-O.
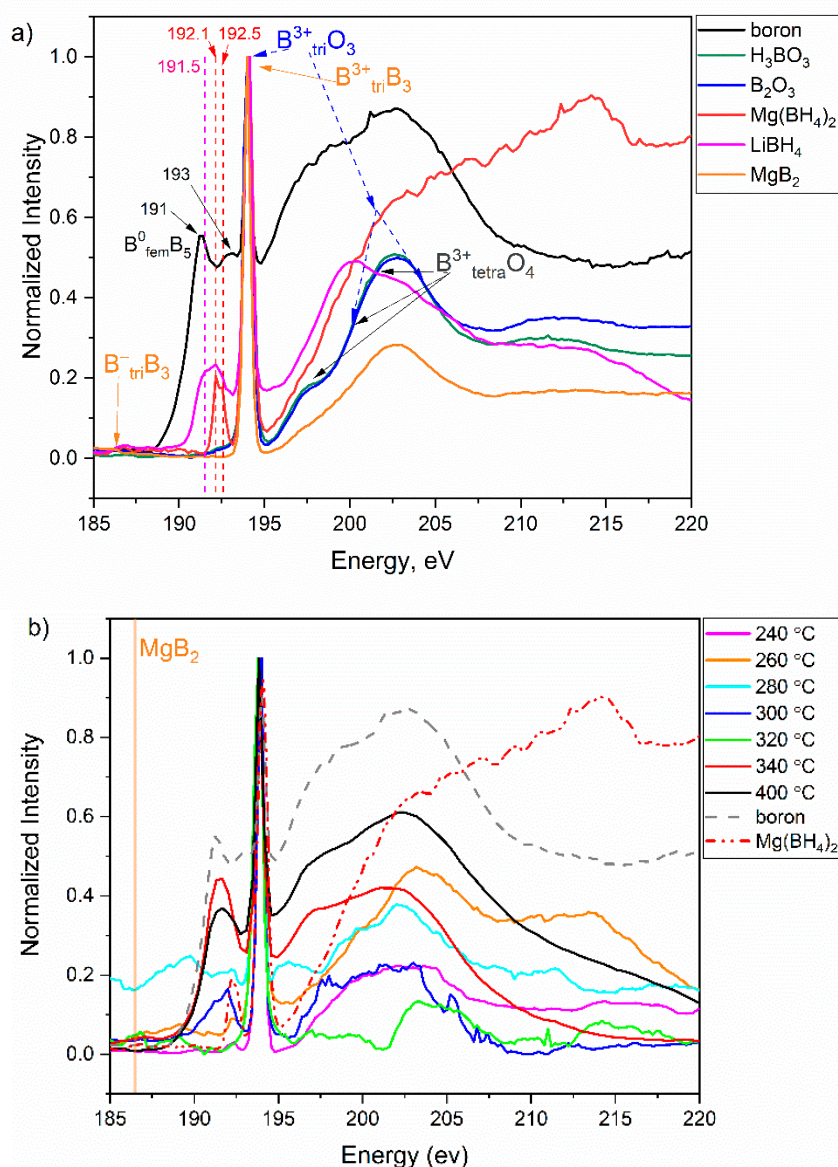

Figure 5. B K-edge NEXAFS spectra of (**a**) boron-based reference compounds, (**b**) samples decomposed at various temperatures.

Magnesium boride, MgB_2, has a hexagonal layered structure (space group P_6/mmm) with boron honeycomb sheets interlaying with the Mg triangular sheets. Thus, boron atoms are covalently bound to three neighboring B in-plane and have a formal oxidation state -1. Hybridization of p_x and p_y orbitals of B atoms results in the formation of two strong covalent σ bonds. In addition, B p_z orbitals form a π-bond with the 3s states of Mg [50]. Theory predicts an edge at 186.8 eV as a result of $2p_{xy}$ unoccupied final states above the Fermi level of MgB_2 [28], but a very weak peak was observed here (Figure 5a, orange curve). According to Ray et al., this can be explained by oxidation of the sample. Indeed, the spectrum of MgB_2 is dominated by the peak at 194 eV [28]. The peak at 186.8 eV, however, was considered a fingerprint for the formation of MgB_2.

The spectrum of the amorphous boron closely resembles that of the crystalline β-B_{105} phase [51] reflecting a similar local structure of B_{12} icosahedra where each boron atom is coordinated to five neighbors. The sharp feature at 194 eV stems from contamination with

B_{tri}-O species as the spectra reported in literature do not contain such a peak [46]. The edge energy of 188 eV is lower than that in oxides, as expected, due to the lower oxidation state of boron with no formal charge. The peaks at 191 and 193 eV are characteristic of this structure.

The spectrum of $LiBH_4$ was measured along with $Mg(BH_4)_2$ to investigate the common features of BH_4^- ions in NEXAFS. In $LiBH_4$ and $Mg(BH_4)_2$, boron in sp^3 hybridization is tetrahedrally coordinated to four H atoms. Interestingly, both the borohydrides have a peak at ca. 192 eV. However, the peaks have a complex and different structure, evidencing variations in the local environment of boron atoms. For example, a lower-energy shift in $LiBH_4$ may suggest less positive charge of boron atoms. The spectral structure of γ-$Mg(BH_4)_2$ (Figure 5a, red spectrum) with the first peak at about 192 eV and the sharp peak at 193 eV showed tetrahedral B coordination in BH_4^- as earlier studied by Jeong et al. [29].

Figure 5b shows NEXAFS spectra of decomposed $Mg(BH_4)_2$. One can immediately note that all the spectra demonstrate peaks due to boron oxides with planar anions evidencing sample oxidation.

At the same time, the region at 187–197 eV contains the information on other boron species. The spectra for the samples decomposed at 240 °C and 260 °C both showed the peak at 192 eV for the tetrahedral coordination of boron in BH_4^- suggesting $Mg(BH_4)_2$ residuals. The spectrum of the sample decomposed at 280 °C also showed a weak feature in that region. Other than that, the spectrum is of a rather poor quality, making it difficult to extract further conclusions. In the next spectrum (300 °C) we can observe a rather strong complex peak at ca. 192 eV, at the energies between those of amorphous boron and $Mg(BH_4)_2$. This suggests the presence of boron species in a lower oxidation state than in the $(BH_4)^-$ and closer to zero. That feature disappears in the 320 °C sample though it is also possible that this sample is oxidised to a larger extent. The spectra of the 340 °C and 400 °C samples demonstrate, again, a strong broad peak at 191.6 eV of a slightly different shape. Together with the spectrum profile above 195 eV, these spectra are very similar to those of the amorphous boron with some difference in the structure of the 191.6 eV peak. MgB_2 was not found in the studied samples. However, this might also be due to the fact that the species was not present in the oxidised surface layer probed by TEY.

It can be noted that the different quality of the spectra might evidence different electronic properties of the samples as the data quality depends on the sample's conductivity. Among those, the phases obtained at 280–320 °C have the worst quality and perhaps lowest conductivity. For higher decomposition temperatures, the noise decreases again. On the other hand, the noise can also be associated with the larger heterogeneity of the species in the 280–320 °C range.

4. Discussion and Conclusions

With a multi-technique experimental approach, we have analyzed different reaction phases in the partial decomposition of γ-$Mg(BH_4)_2$ in an Ar atmosphere. A maximum of 12% weight loss at 400 °C was measured by thermogravimetry, with the production of amorphous B-H species. Although no analysis of the desorbed gaseous species was carried out, the overall weight loss suggests that the main released gas was hydrogen since the desorption of boron species would correspond to larger weight losses. PXRD confirmed the absence of crystalline compounds in the partially decomposed samples at 260–280 °C temperatures, and formation of MgH_2 after decomposition at 300 °C with the subsequent incomplete decomposition to Mg until 400 °C. Formation of MgB_2 was not observed with PXRD and NEXAFS. SR-FTIR in transmission mode indicated the formation of bridged B-H-B species in the partially decomposed samples at 260–280 °C as well as the presence of several amorphous phases. Some contamination of the sample was observed, evidenced by the peaks of MgO in the PXRD patterns after 320 °C and boron oxide species in the NEXAFS and FTIR spectra. In the far-FTIR spectra, the peaks at the positions similar to that of H_3BO_3 were weak in the pure $Mg(BH_4)_2$ and more intense in the samples decomposed at 260–280 °C. To the best of our knowledge, we reported, for the first time in situ, (300–10 K)

far-FTIR spectra of H_3BO_3 and $Mg(BH_4)_2$. Combining the results from TGA-DSC, NEXAFS spectrum at boron K-edge, and the PXRD report, the sample when decomposed from 240–300 °C comprises the tetrahedral coordination of B probably in terms of BH_4^- ions and $B_{4-x}H_x$ species. The sample decomposed at 300 °C shows boron in oxidation states between those in $(BH_4)^-$ and amorphous boron. Summarizing, our combined experimental approach added more insights to the decomposition reaction of γ-$Mg(BH_4)_2$ in Ar for the equilibrium reaction products as collected in Table 5:

Table 5. Summary of the study of decomposition products of γ-$Mg(BH_4)_2$ in Ar.

T_{dec} (°C)	Maximum Weight Loss, wt% (TGA)	Released No. of H_2 Molecules	Nominal Composition after H_2 Desorption	Reaction Step (TGA-DSC)	Crystalline Reaction Products (PXRD)	FTIR	NEXAFS
240	2.1	1.1	MgB_2H_7	I	ht-$Mg(BH_4)_2$	n/a	B_{tri}-O, $(BH_4)^-$
260	4.5	2.4	$MgB_2H_{5.6}$	I	No	- several B_xH_y phases- B-H-B	B_{tri}-O, $(BH_4)^-$
280	5.2	2.8	$MgB_2H_{5.2}$	I	No	species - B_3-B_5 clusters	B_{tri}-O
300	8.8	4.7	$MgB_2H_{3.3}$	I	MgH_2	n/a	B_{tri}-O, boron species between $(BH_4)^-$ and B^0
320	9.9	5.3	$MgB_2H_{2.8}$	II	Mg, MgO	n/a	B_{tri}-O
340	11.6	6.2	$MgB_2H_{1.8}$	III, IV	Mg, MgO	n/a	B_{tri}-O, B^0
400	12	6.5	$MgB_2H_{1.5}$	IV	Mg, MgO	n/a	B_{tri}-O, B^0

This constitutes a further step in the knowledge of the very complex decomposition mechanism of this attractive hydrogen storage material.

Author Contributions: Conceptualization, O.Z.; methodology, O.Z.; data analysis, R.D., J.G.V. and O.Z.; investigation (synchrotron experiments): all authors; resources: S.D., O.Z.; writing—original draft preparation, R.D., J.G.V. and O.Z.; writing—review and editing, all authors; visualization, O.Z., J.G.V., R.D.; supervision, O.Z.; project administration, O.Z.; funding acquisition: O.Z. All authors have read and agreed to the published version of the manuscript.

Institutional Review Board Statement: Not applicable.

Informed Consent Statement: Not applicable.

Data Availability Statement: The data supporting the conclusions of this manuscript will be made available by the authors, without undue reservation, to any qualified researcher.

Conflicts of Interest: The authors declare no conflict of interest.

References

1. Rifkin, J. *The Hydrogen Economy: The Creation of the Worldwide Energy Web and the Redistribution of Power on Earth*; Wiley: New York, NY, USA, 2002; p. 304.
2. Lovisolo, L.; Serdoner, A.; Whiriskey, K.; Larsson, R. *Electrolysis Hydrogen Production in Europe*; Bellona Europa, 2021. Available online: https://network.bellona.org/content/uploads/sites/3/2021/04/Electrolysis-Hydrogen-Production-In-Europe-5.pdf (accessed on 10 August 2022).
3. Andersson, J.; Grönkvist, S. Large-scale storage of hydrogen. *Int. J. Hydrogen Energy* **2019**, *44*, 11901–11919. [CrossRef]
4. Hydrogen and Fuel Cell Technologies Office. Hydrogen Storage- Basics. Available online: https://www.energy.gov/eere/fuelcells/hydrogen-storage (accessed on 10 August 2022).
5. Mohtadi, R.; Orimo, S.-I. The renaissance of hydrides as energy materials. *Nat. Rev. Mater.* **2016**, *2*, 16091. [CrossRef]

6. Rivard, E.; Trudeau, M.; Zaghib, K. Hydrogen Storage for Mobility: A Review. *Materials* **2019**, *12*, 1973. [CrossRef] [PubMed]

7. Yartys, V.A.; Lototsky, M.V. An Overview of Hydrogen Storage Methods. In *Hydrogen Materials Science and Chemistry of Carbon Nanomaterials*; Veziroglu, T.N., Yu. Zaginaichenko, S., Schur, D.V., Baranowski, B., Shpak, A.P., Skorokhod, V.V., Eds.; Springer: Dordrecht, The Netherlands, 2005; pp. 75–104.

8. Dematteis, E.M.; Amdisen, M.B.; Autrey, T.; Barale, J.; Bowden, M.E.; Buckley, C.E.; Cho, Y.W.; Deledda, S.; Dornheim, M.; de Jongh, P.; et al. Hydrogen storage in complex hydrides: Past activities and new trends. *Prog. Energy* **2022**, *4*, 032009. [CrossRef]

9. Chong, M.; Karkamkar, A.; Autrey, T.; Orimo, S.; Jalisatgi, S.; Jensen, C.M. Reversible dehydrogenation of magnesium borohydride to magnesium triborane in the solid state under moderate conditions. *Chem. Commun.* **2011**, *47*, 1330–1332. [CrossRef] [PubMed]

10. Zavorotynska, O.; El-Kharbachi, A.; Deledda, S.; Hauback, B.C. Recent progress in magnesium borohydride $Mg(BH_4)_2$: Fundamentals and applications for energy storage. *Int. J. Hydrogen Energy* **2016**, *41*, 14387–14403. [CrossRef]

11. Zavorotynska, O.; Deledda, S.; Li, G.Q.; Matsuo, M.; Orimo, S.; Hauback, B.C. Isotopic Exchange in Porous and Dense Magnesium Borohydride. *Angew. Chem. Int. Ed.* **2015**, *54*, 10592–10595. [CrossRef]

12. Heere, M.; Zavorotynska, O.; Deledda, S.; Sorby, M.H.; Book, D.; Steriotis, T.; Hauback, B.C. Effect of additives, ball milling and isotopic exchange in porous magnesium borohydride. *RSC Adv.* **2018**, *8*, 27645–27653. [CrossRef]

13. Guo, S.; Chan, H.; Reed, D.; Book, D. Investigation of dehydrogenation processes in disordered $\gamma\text{-}Mg(BH_4)_2$. *J. Alloys Compd.* **2013**, *580*, S296–S300. [CrossRef]

14. Hanada, N.; Chłopek, K.; Frommen, C.; Lohstroh, W.; Fichtner, M. Thermal decomposition of $Mg(BH_4)_2$ under He flow and H_2 pressure. *J. Mater. Chem.* **2008**, *18*, 2611–2614. [CrossRef]

15. Li, H.W.; Kikuchi, K.; Nakamori, Y.; Miwa, K.; Towata, S.; Orimo, S. Effects of ball milling and additives on dehydriding behaviors of well-crystallized $Mg(BH_4)_2$. *Scr. Mater.* **2007**, *57*, 679–682. [CrossRef]

16. Paskevicius, M.; Pitt, M.P.; Webb, C.J.; Sheppard, D.A.; Filsø, U.; Gray, E.M.; Buckley, C.E. In-Situ X-ray Diffraction Study of $\gamma\text{-}Mg(BH_4)_2$ Decomposition. *J. Phys. Chem. C* **2012**, *116*, 15231–15240. [CrossRef]

17. Soloveichik, G.L.; Gao, Y.; Rijssenbeek, J.; Andrus, M.; Kniajanski, S.; Bowman, R.C.; Hwang, S.-J.; Zhao, J.-C. Magnesium borohydride as a hydrogen storage material: Properties and dehydrogenation pathway of unsolvated $Mg(BH_4)_2$. *Int. J. Hydrogen Energy* **2009**, *34*, 916–928. [CrossRef]

18. Vitillo, J.G.; Bordiga, S.; Baricco, M. Spectroscopic and Structural Characterization of Thermal Decomposition of $\gamma\text{-}Mg(BH_4)_2$: Dynamic Vacuum versus H_2 Atmosphere. *J. Phys. Chem. C* **2015**, *119*, 25340–25351. [CrossRef]

19. Zavorotynska, O.; Saldan, I.; Hino, S.; Humphries, T.D.; Deledda, S.; Hauback, B.C. Hydrogen cycling in $\gamma\text{-}Mg(BH_4)_2$ with cobalt-based additives. *J. Mater. Chem. A* **2015**, *3*, 6592–6602. [CrossRef]

20. Zavorotynska, O.; Deledda, S.; Vitillo, J.G.; Saldan, I.; Guzik, M.N.; Baricco, M.; Walmsley, J.C.; Muller, J.; Hauback, B.C. Combined X-ray and Raman Studies on the Effect of Cobalt Additives on the Decomposition of Magnesium Borohydride. *Energies* **2015**, *8*, 9173–9190. [CrossRef]

21. Newhouse, R.J.; Stavila, V.; Hwang, S.-J.; Klebanoff, L.E.; Zhang, J.Z. Reversibility and Improved Hydrogen Release of Magnesium Borohydride. *J. Phys. Chem. C* **2010**, *114*, 5224–5232. [CrossRef]

22. Yan, Y.; Remhof, A.; Rentsch, D.; Züttel, A. The role of $MgB12H12$ in the hydrogen desorption process of $Mg(BH_4)_2$. *Chem. Commun.* **2015**, *51*, 700–702. [CrossRef]

23. Zavorotynska, O.; Sorby, M.H.; Vitillo, J.G.; Deledda, S.; Frommen, C.; Hauback, B.C. Experimental and computational characterization of phase transitions in CsB_3H_8. *Phys. Chem. Chem. Phys.* **2021**, *23*, 17836–17847. [CrossRef]

24. Sethio, D.; Daku, L.M.L.; Hagemann, H.; Kraka, E. Quantitative Assessment of B-B-B, B-H(b) -B, and B-H(t) Bonds: From BH(3) to B(12) H(12) (2). *Chemphyschem* **2019**, *20*, 1967–1977. [CrossRef]

25. Severa, G.; Rönnebro, E.; Jensen, C.M. Direct hydrogenation of magnesium boride to magnesium borohydride: Demonstration of >11 weight percent reversible hydrogen storage. *Chem. Commun.* **2010**, *46*, 421–423. [CrossRef] [PubMed]

26. Zavorotynska, O.; Deledda, S.; Hauback, B.C. Kinetics studies of the reversible partial decomposition reaction in $Mg(BH_4)_2$. *Int. J. Hydrogen Energy* **2016**, *41*, 9885–9892. [CrossRef]

27. Saldan, I.; Hino, S.; Humphries, T.D.; Zavorotynska, O.; Chong, M.; Jensen, C.M.; Deledda, S.; Hauback, B.C. Structural Changes Observed during the Reversible Hydrogenation of Mg(BH4)(2) with Ni-Based Additives. *J. Phys. Chem. C* **2014**, *118*, 23376–23384. [CrossRef]

28. Ray, K.G.; Klebanoff, L.E.; Lee, J.R.I.; Stavila, V.; Heo, T.W.; Shea, P.; Baker, A.A.; Kang, S.; Bagge-Hansen, M.; Liu, Y.-S.; et al. Elucidating the mechanism of MgB_2 initial hydrogenation via a combined experimental–theoretical study. *Phys. Chem. Chem. Phys.* **2017**, *19*, 22646–22658. [CrossRef] [PubMed]

29. Jeong, S.; Heo, T.; Oktawiec, J.; Shi, R.; Kang, S.; White, J.; Schneemann, A.; Zaia, E.; Wan, L.; Ray, K.; et al. A Mechanistic Analysis of Phase Evolution and Hydrogen Storage Behavior in Nanocrystalline $Mg(BH_4)_2$ within Reduced Graphene Oxide. *ACS Nano* **2020**, *14*, 1745–1756. [CrossRef]

30. Sahle, C.J.; Kujawski, S.; Remhof, A.; Yan, Y.; Stadie, N.P.; Al-Zein, A.; Tolan, M.; Huotari, S.; Krisch, M.; Sternemann, C. In situ characterization of the decomposition behavior of $Mg(BH_4)_2$ by X-ray Raman scattering spectroscopy. *Phys. Chem. Chem. Phys.* **2016**, *18*, 5397–5403. [CrossRef]

31. Solovev, M.V.; Chashchikhin, O.V.; Dorovatovskii, P.V.; Khrustalev, V.N.; Zyubin, A.S.; Zyubina, T.S.; Kravchenko, O.V.; Zaytsev, A.A.; Dobrovolsky, Y.A. Hydrolysis of $Mg(BH_4)_2$ and its coordination compounds as a way to obtain hydrogen. *J. Power Sources* **2018**, *377*, 93–102. [CrossRef]

32. Jun, L.; Shuping, X.; Shiyang, G. FT-IR and Raman spectroscopic study of hydrated borates. *Spectrochim. Acta Part A Mol. Biomol. Spectrosc.* **1995**, *51*, 519–532. [CrossRef]

33. Nakamoto, K. Applications in Inorganic Chemistry. In *Infrared and Raman Spectra of Inorganic and Coordination Compounds*, 6th ed.; John Wiley & Sons: Hoboken, NJ, USA, 2008; Volume A, pp. 149–354.

34. Mirabella, F.M. Principles, Theory and Practice of Internal Reflection Spectroscopy. In *Handbook of Vibrational Spectroscopy*; John Wiley & Sons, Ltd.: New York, NY, USA, 2006.

35. Chong, M.; Autrey, T.; Jensen, C.M. Lewis Base Complexes of Magnesium Borohydride: Enhanced Kinetics and Product Selectivity upon Hydrogen Release. *Inorganics* **2017**, *5*, 89. [CrossRef]

36. Gigante, A.; Leick, N.; Lipton, A.S.; Tran, B.; Strange, N.A.; Bowden, M.; Martinez, M.B.; Moury, R.; Gennett, T.; Hagemann, H.; et al. Thermal Conversion of Unsolvated $Mg(B_3H_8)_2$ to BH_4- in the Presence of MgH_2. *ACS Appl. Energy Mater.* **2021**, *4*, 3737–3747. [CrossRef]

37. Palumbo, O.; Nguyen, P.; Jensen, C.M.; Paolone, A. Determination of the molecular structure of amorphous $Mg(B_3H_8)_2(THF)_2$ through infrared spectroscopic and computational studies. *Int. J. Hydrogen Energy* **2016**, *41*, 5986–5993. [CrossRef]

38. Matsui, Y.; Taylor, R.C. Vibrational spectra and structure of the heptahydrodiborate ion, [B2H7]− in glycol ethers. *Spectrochim. Acta Part A Mol. Spectrosc.* **1989**, *45*, 299–304. [CrossRef]

39. Lutz, C.A.; Ritter, D.M. Observations on alkylboranes. *Can. J. Chem.* **1963**, *41*, 1344–1358. [CrossRef]

40. Hrostowski, H.J.; Pimentel, G.C. The Infrared Spectra of Stable Pentaborane and Deuterated Pentaborane. *J. Am. Chem. Soc.* **1954**, *76*, 998–1003. [CrossRef]

41. Johnson, H.D.; Geanangel, R.A.; Shore, S.G. Alkali metal salts derived from pentaborane(9) and hexaborane(10): MB5H8 and MB6H9. *Inorg. Chem.* **1970**, *9*, 908–912. [CrossRef]

42. Brint, P.; Sangchakr, B.; Fowler, P.W.; Weldon, V.J. Bonding in clusters Part 10. The nature of the bh groups in closo-borane anions—A study by vibrational spectroscopy, electronic spectroscopy for chemical-analysis, and abinitio computation. *J. Chem. Soc. Dalton Trans.* **1989**, *11*, 2253–2260. [CrossRef]

43. Leites, L.A. Vibrational spectroscopy of carboranes and parent boranes and its capabilities in carborane chemistry. *Chem. Rev.* **1992**, *92*, 279–323. [CrossRef]

44. Erbil, A.; Cargill, G.S.; Frahm, R.; Boehme, R.F. Total-electron-yield current measurements for near-surface extended X-ray-absorption fine-structure. *Phys. Rev. B* **1988**, *37*, 2450–2464. [CrossRef]

45. Esposto, F.J.; Aebi, P.; Tyliszczak, T.; Hitchcock, A.P.; Kasrai, M.; Bozek, J.D.; Jackman, T.E.; Rolfe, S.R. Boron K-shell spectroscopy of boron-doped silicon. *J. Vac. Sci. Technol. A* **1991**, *9*, 1663–1669. [CrossRef]

46. Blau, W.; Dudde, R.; Petersen, H. Photoyield measurements of the boron k-edge fine structure of amorphous Fe80B20 alloys. *Solid State Commun.* **1989**, *69*, 147–150. [CrossRef]

47. Henderson, G.S.; de Groot, F.M.F.; Moulton, B.J.A. X-ray Absorption Near-Edge Structure (XANES) Spectroscopy. *Rev. Mineral. Geochem.* **2014**, *78*, 75–138. [CrossRef]

48. Ishiguro, E.; Iwata, S.; Suzuki, Y.; Mikuni, A.; Sasaki, T. The boron K photoabsorption spectra of BF_3, BCl_3, and BBr_3. *J. Phys. B At. Mol. Phys.* **1982**, *15*, 1841–1854. [CrossRef]

49. Fleet, M.E.; Muthupari, S. Boron K-edge XANES of borate and borosilicate minerals. *Am. Mineral.* **2000**, *85*, 1009–1021. [CrossRef]

50. Guerfi, T. Out-of-plane ionicity versus in-plane covalency interplay and electron–phonon coupling in MgB_2 superconductor. *Chin. J. Phys.* **2020**, *64*, 287–294. [CrossRef]

51. Li, D.; Bancroft, G.M.; Fleet, M.E. B K-edge XANES of crystalline and amorphous inorganic materials. *J. Electron Spectrosc. Relat. Phenom.* **1996**, *79*, 71–73. [CrossRef]

52. Peatman, W.; Schade, U. A brilliant infrared light source at BESSY. *Rev. Sci. Instrum.* **2001**, *72*, 1620–1624. [CrossRef]